



# Enhancement of photocatalytic H<sub>2</sub> evolution on pyrene-based polymer promoted by MoS<sub>2</sub> and visible light

Shaohong Zang, Guigang Zhang, Zhi-An Lan, Dandan Zheng, Xinchen Wang<sup>\*,1</sup>

State Key Laboratory of Photocatalysis on Energy and Environment, College of Chemistry, Fuzhou University, Fuzhou, 350116, PR China



## ARTICLE INFO

**Keywords:**  
Photocatalysis  
Heterojunction  
Pyrene-based conjugated polymer  
MoS<sub>2</sub>  
H<sub>2</sub> production

## ABSTRACT

Conjugated polymers have gathered particular interests in photocatalysis because of their excellent properties such as optimization flexibility, cost-effective, and robust stability. The pyrene-based polymer (PyP), as one of the conjugated polymers, holds a great potential for water splitting because of their suitable band structure, visible light absorption, and high surface area. However, because of the fast charge carrier recombination confined by Frenkel excitons with high exciton binding energy, PyP in its pristine form remains barely active for photocatalytic hydrogen evolution. The concise construction of heterojunction is a feasible way to accelerate the charge separation, increase the lifetime of the photogenerated e<sup>-</sup>/h<sup>+</sup> pair and decrease the activation barriers of hydrogen evolution reaction. In this work, a series of transition metal sulfides as cocatalysts have been deposited on PyP to construct heterojunctions for photocatalytic H<sub>2</sub> evolution reaction (HER). The loading techniques (immersion, in-situ and photodeposition) and the loading contents of cocatalysts have been investigated. The optimized MoS<sub>2</sub>/PyP sample exhibited a 10-fold increase in comparison with pure PyP without modification. The extended  $\pi$ -conjugation, high surface area, and widely exposed 2D interface highlight the importance of PyP as effective supports for stabilizing the homogeneously dispersed MoS<sub>2</sub>, thereby resulting in an efficient photocatalytic activity. This study provides a new idea to construct low-cost, sustainable and efficient hybrid system for photocatalytic hydrogen production.

## 1. Introduction

Photocatalytic water splitting for hydrogen production using semiconductor is an ideal potential solution to replace the traditional fossil fuels and to decrease the harmful effects of the flue gases [1–3]. With this perspective, design and synthesis of semiconductors that possess suitable band position and favorable stability for efficient water splitting is of particular importance. Recently, organic conjugated polymers (OCPs) with sufficient visible light absorption are highly concerned for photocatalytic water splitting to hydrogen; despite they are known as organic semiconductors applied to devices such as solar cells, organic LEDs, microactuators, and sensors previously [4–7].

The work of OCPs for photocatalytic water splitting can date back to 1985, while linear poly(p-phenylene)s shows H<sub>2</sub> evolution activity under ultraviolet light irradiation [8]. This discovery inspired the development of conjugated polymers for photocatalytic water splitting, but their unfavorable stability and lack of visible light response extremely restrict the activity. The study on this research topic almost stops for ca. 30 years till 2009 when carbon nitride polymer

photocatalyst was discovered. Polymeric carbon nitride (PCN) is a good supplementary to the conjugated polymers' family. It exhibits robust stability and is able to capture visible photons, making it promising photocatalyst for photocatalytic water splitting [9]. Nevertheless, the photocatalytic activity of pristine PCN is still inefficient because of the fast recombination rate of the photogenerated charge carriers and absence of light absorption above 460 nm [10]. Subsequently in 2015, the fabrication of various conjugated microporous polymers (CP-CMPs) by Cooper's group with different visible light absorption and enhanced photocatalytic hydrogen activity further stimulates the development of OCPs for photocatalytic water splitting [11]. The most prominent one, pyrene-benzene polymer (named as PyP), synthesized from copolymerization of 1,4-Phenylenebisboronic acid and 1,3,6,8-tetrabromopyrene co-monomers via the typical Suzuki-Miyaura reaction. Specifically, PyP shows an excellent visible light absorption (wavelength < 520 nm) because of the narrow band gap of 2.3 eV.

Despite all of these advantages, PyP in its pristine form remains barely active for HER because of the fast charge carrier recombination, leading to low quantum yield of charge carriers arriving at the

\* Corresponding author.

E-mail address: [xcwang@fzu.edu.cn](mailto:xcwang@fzu.edu.cn) (X. Wang).

<sup>1</sup> [Http://wanglab.fzu.edu.cn](http://wanglab.fzu.edu.cn).

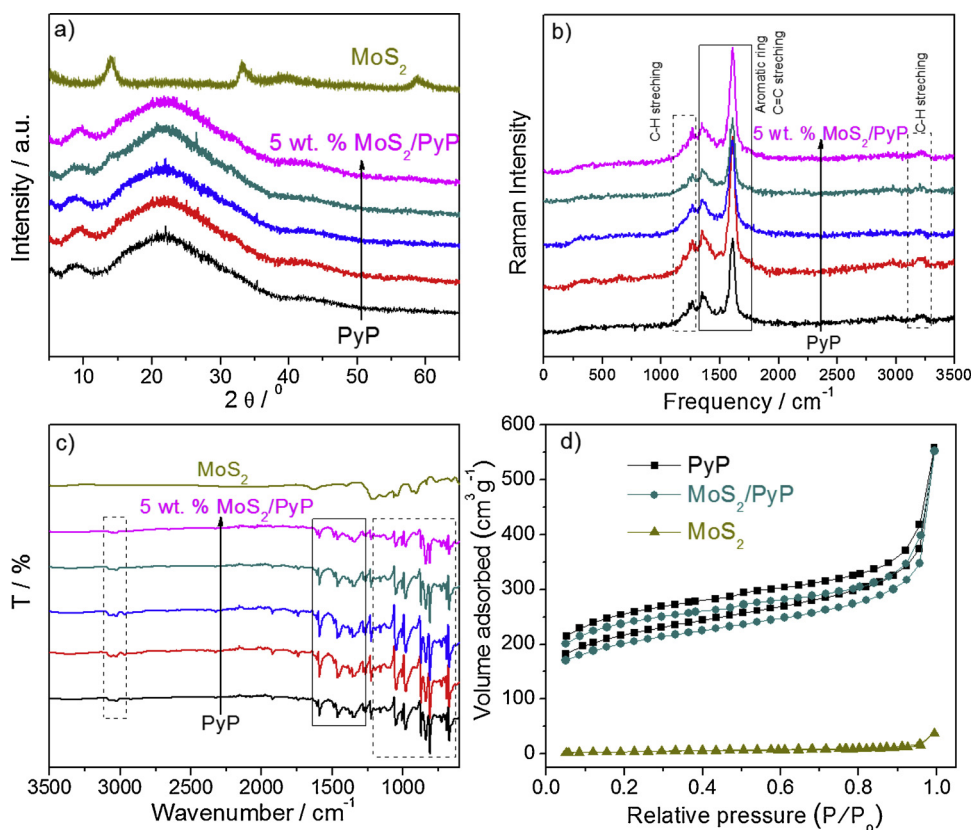


**Fig. 1.** (a) XRD patterns, (b) Raman spectra (c) FT-IR spectra of x wt. % MoS<sub>2</sub>/PyP(IM) samples, (d) N<sub>2</sub> adsorption-desorption isotherms of pure PyP and MoS<sub>2</sub>, and 3 wt. % MoS<sub>2</sub>/PyP(IM) samples.

interface. One of the inherent reasons is because photoexcitation in organic semiconductors usually generates Frenkel excitons with high exciton binding energy leading to the lack of active sites on the PyP's surface [12]. Beyond that, the amorphous form of PyP means disorder in structure and abundance of defects, which also leads to the rapid charge carrier recombination making surface water reduction reactions with low activity. One can easily imagine that the activity of the polymer will be further promoted after a rational modification of the polymers.

To address these issues of OCPs, most studies are focused on designing more and more complicated new structures by organic reactions, including of poly(triazine)/heptazine-, fluorine-type, bipyridyl-, benzothiadiazole-, and thiophene-based polymers [13–17]. Although molecular structure regulation of OCPs can ameliorate the high exciton binding energy or the visible light absorption, the activity of H<sub>2</sub> evolution is still bothered by the fast charge carrier recombination and high activation barriers [18–20]. Constructing heterojunctions is considered one of the most efficient strategies which not only enhances visible light absorption but also promotes the transfer of photogenerated charge carriers caused by their negligible overpotential and excellent kinetics [12c,21–23]. Therefore, development of suitable materials to construct heterojunctions with PyP for photocatalytic H<sub>2</sub> evolution is therefore of great value. With dense active sites and an electronic conductivity, transition metals show excellent performance in photocatalytic system [24]. Among them, MoS<sub>2</sub> consisting of a layered S-Mo-S structure in an octahedral lattice, has been extensively investigated for electrocatalytic and powdered photocatalytic hydrogen evolution [25,29]. Previously, MoS<sub>2</sub>-TiO<sub>2</sub>, MoS<sub>2</sub>-CdS, MoS<sub>2</sub>-RGO and MoS<sub>2</sub>-PCN being reported mean that MoS<sub>2</sub> has good performance because of good electronic conductivity and offering active sites [26–29]. Moreover, the existence of π-conjugation structure in PyP, it is beneficial to interact with the lamellar structure MoS<sub>2</sub> to enhance the charge transfer between them and

inhibit the recombination of electrons and holes.

Herein, taking its geometrical and electronic advantages into consideration, MoS<sub>2</sub> is rationally loaded onto the surface of PyP to construct an organic-inorganic heterojunction for improving H<sub>2</sub> production activity. We expect that the distinct nanoscale structure of MoS<sub>2</sub> can increase the accessible area around the PyP's interface and decrease the barrier for electron transport, thus facilitating the electron transfer across the interface by the electron tunneling effect and offering more active sites. Construction of the MoS<sub>2</sub>/PyP heterojunction was prepared via facile immersion, photodeposition and in-situ method (named as MoS<sub>2</sub>/PyP(IM), MoS<sub>2</sub>/PyP(PD), MoS<sub>2</sub>/PyP(IS), where IM, PD, and IS represent the fabrication techniques). The characterization results indicate that MoS<sub>2</sub>/PyP(IM) shows optimum photoactivity. The effect of other transition metal sulfides (FeS<sub>2</sub>, CoS<sub>2</sub>, NiS<sub>2</sub>) for PyP (MS<sub>2</sub>/PyP) were also investigated and all the as-prepared composites showed good photocatalytic H<sub>2</sub> production activity. Therefore, the MS<sub>2</sub>/PyP heterojunctions is desirable as, in principle, can improve the photocatalytic hydrogen production activity. In addition, to gain further insight into the photocatalytic mechanism of the heterostructure, the photoelectrochemical properties of pure PyP and MoS<sub>2</sub>/PyP(IM) have been further carried out. We believe that it should provide a choice to develop new materials like PyP-based photocatalysts for hydrogen evolution reaction.

## 2. Experimental

### 2.1. Preparation of PyP

A flask was charged with the monomers, 1,4-Benzene diboronic acid (3.5 mmol), 1,3,6,8-tetrabromopyrene (7.0 mmol), using Pd(PPh<sub>3</sub>)<sub>4</sub> (0.8 mol%) as a catalyst in N,N-dimethylformamide (50 ml) and aqueous K<sub>2</sub>CO<sub>3</sub> (2 M, 10 ml) with stirring to mix the monomers evenly.

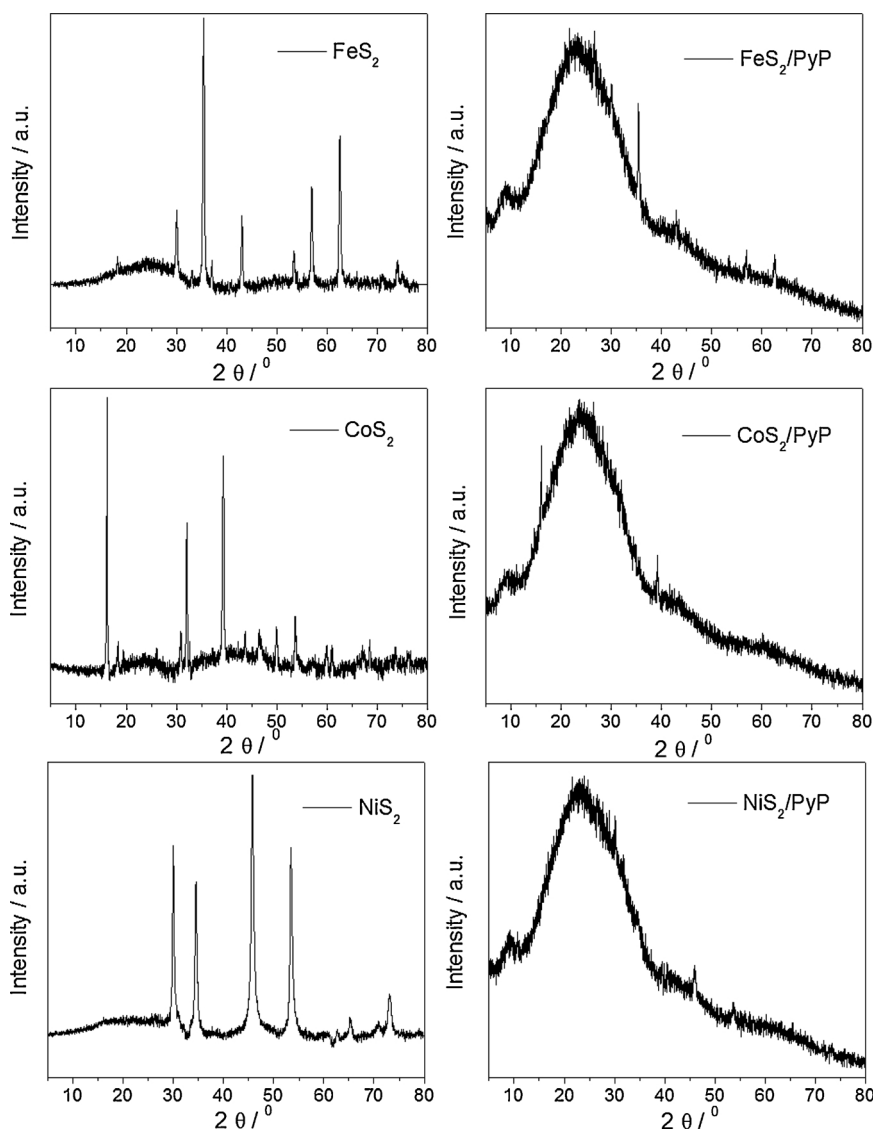


Fig. 2. XRD patterns of pure  $MS_2$  and 3 wt. %  $MS_2/PyP$  (IM) samples.

Then the mixture was degassed by Ar for 30 min, and the reaction was carried out at 150 °C for 48 h. After work-up, the mixture was taken out and washed thoroughly with deionized water and methanol. The product was further purified by Soxhlet extraction with tetrahydrofuran for 2 days and finally dried in a vacuum oven [11].

## 2.2. Preparation of $MoS_2$

$MoS_2$  was prepared by typical hydrothermal method [25]. Sodium molybdate dihydrate ( $Na_2MoO_4 \cdot 2H_2O$ ) and thiourea (molar ratio = 1:2) were put into 60 mL distilled water with magnetic stirring. After completely resolved, the mixture reacted in a 100 mL Teflon-lined stainless steel autoclave at 200 °C for 12 h. After cooling, the resulting product was collected, washed with distilled water three times, and finally dried at 60 °C.

## 2.3. Fabrication of and $MoS_2/PyP$

Immersion method ( $MoS_2/PyP$ (IM)): 0.2 g PyP was immersed into 4 mL aqueous solutions with different amounts of  $MoS_2$ . The mixture was stirred and ultrasonication for 10 min. The final sample was obtained after evaporation and dried.

In-situ method ( $MoS_2/PyP$ (IS)) :  $MoS_2/PyP$ (IS) was synthesized

under the same condition of  $MoS_2$  with the addition of PyP in the reaction.

Photodeposition [ $MoS_2/PyP$  (PD)]:  $MoS_2/PyP$ (PD) samples was synthesized by photodeposition method. The precursor of  $MoS_2$  is  $(NH_4)_2MoS_4$  which was synthesized according to the literature [30]. Briefly, 1 g ammonium molybdate tetrahydrate ( $(NH_4)_6Mo_7O_{24} \cdot 4H_2O$ ) was added into 15 mL aqueous ammonium sulfide ( $(NH_4)_2S$ , ca. 20 wt. %) and stirred to react completely. And then, the-obtained red precipitate was washed with absolute ethanol and dried in the vacuum oven. For the  $MoS_2/PyP$  (PD), a certain amount of PyP was dispersed in the mixture solution ( $V_{ethanol}:V_{water} = 1:4$ ), then  $(NH_4)_2MoS_4$  was added and stirred for several hours. After being evenly dispersed, the mixture was evacuated several times; the suspension was irradiated under visible light for 1 h. After work-up, the products were filtrated and washed with deionized water several times. After drying, the  $MoS_2/PyP$ (PD) sample were obtained.

## 2.4. Fabrication of and $MS_2/PyP$ ( $M$ is transition metal Fe, Co, Ni)

$MS_2$  was prepared as previously reported work [25,31].  $MCl_2 \cdot nH_2O$  (0.02 mol) and thiourea (molar ratio = 1:2) was added into aqueous ethanediamine (25 ml, 0.187 M). After fully mixed, 30 ml ethanediol was added into the solution, and stirred for 1 h. Then the mixture was

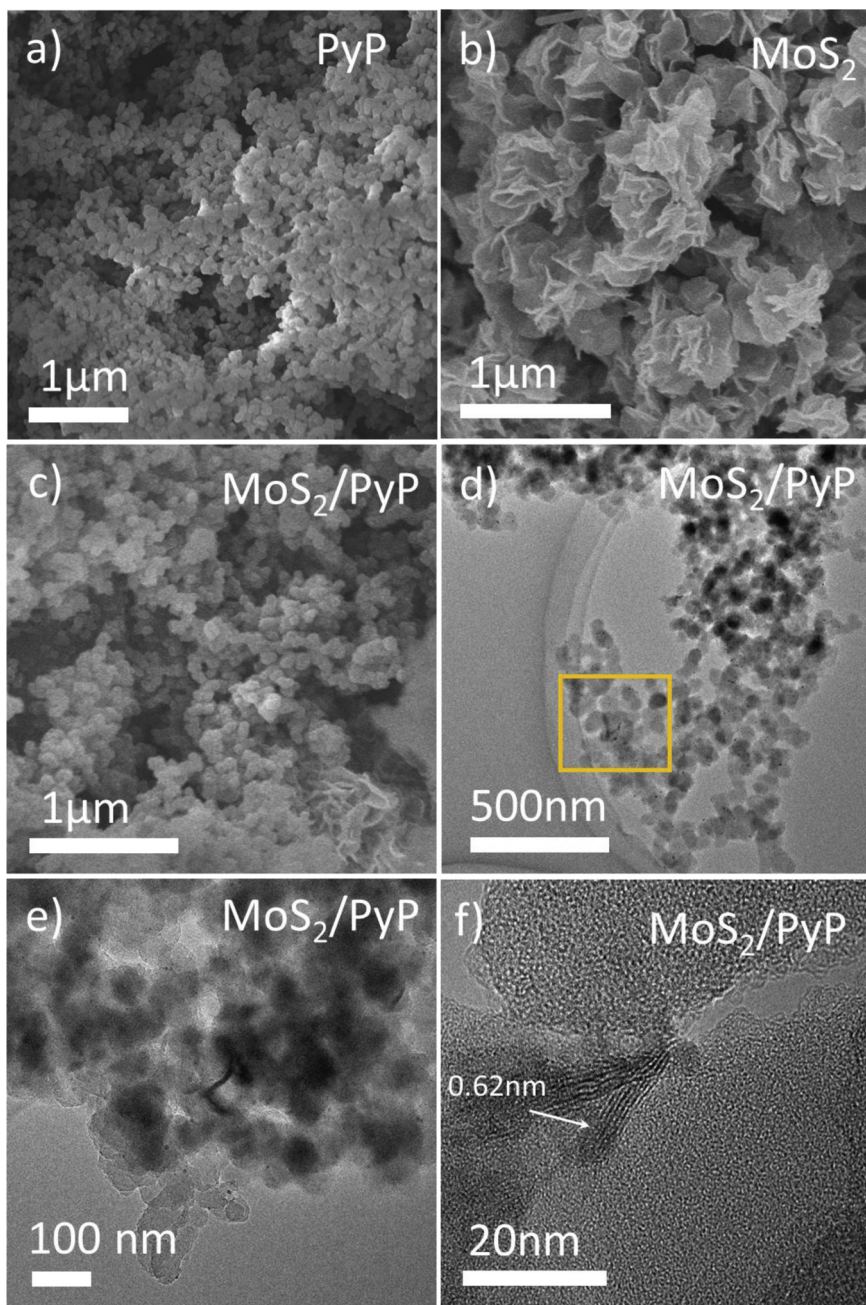


Fig. 3. SEM images of (a) pure PyP, (b) MoS<sub>2</sub> (c) 3 wt. % MoS<sub>2</sub>/PyP(IM) samples; (d, e, f) TEM images of 3 wt. % MoS<sub>2</sub>/PyP(IM) samples.

transferred to the steel autoclave and heated at 180 °C for 12 h. After cooling, the resulted particulate was collected, washed with distilled water three times, and finally dried at 60 °C for overnight.

The MS<sub>2</sub>/PyP was obtained by immersion the same with MS<sub>2</sub>/PyP (IM).

## 2.5. Characterizations

The characterizations of resultant catalysts were carried out by powder XRD, XPS, TEM and FTIR to confirm the composition, structure, and textural properties. The crystal phases of samples were investigated by Powder X-ray diffraction (XRD) measurements on a Bruker D8 Advance diffractometer with Cu-K 1 radiation ( $\lambda = 1.5406 \text{ \AA}$ ). Nitrogen adsorption-desorption isotherms were collected at 77 K using Micromeritics ASAP 2020 Surface Area and Porosity Analyzer. Raman spectra were recorded on a Laser Raman Micrometer (Invia Reflex).

Fourier transform infrared (FT-IR) spectra were recorded on a BioRad FTS 6000 spectrometer. The morphology of the sample was investigated by field emission scanning electron microscopy (SEM) (JSM-6700 F) and transmission electron microscope (TEM) (JEM 2010 EX). X-ray photoelectron spectroscopy (XPS) data were obtained on Thermo ESCALAB250 instrument with a monochromatized Al K $\alpha$  line source (200 W). UV-vis diffuse reflectance spectra (DRS) were performed on a Varian Cary 500 Scan UV-vis system using BaSO<sub>4</sub> as the reference. Photoluminescence spectra (PL) were done on an Edinburgh FI/FSTCSPC 920 spectrophotometer. Electron paramagnetic resonance (EPR) measurements were carried out on a Bruker model A300 spectrometer. Electrochemical measurements were conducted with a BAS Epsilon Electrochemical System in a conventional three electrode cell, using a Pt plate as the counter electrode and an Ag/AgCl electrode (3 M KCl) as the reference electrode. The working electrode was prepared on fluorine-tin oxide (FTO) glass. The 5 mg sample was dispersed in 1 mL

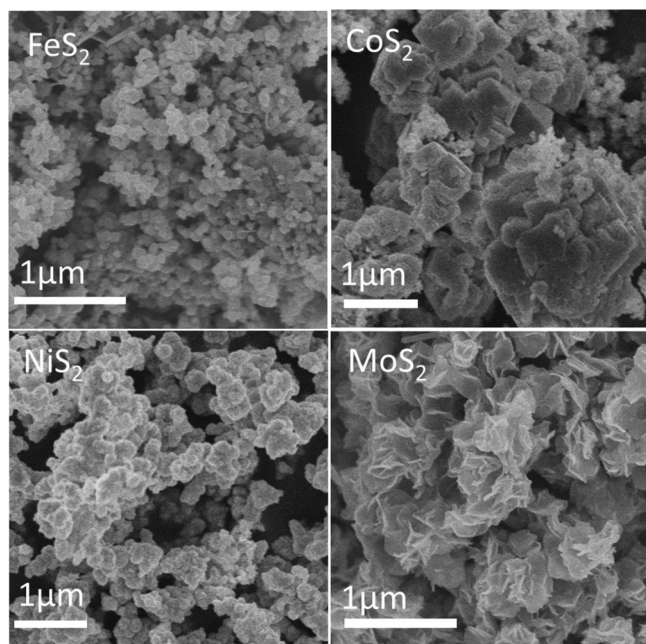


Fig. 4. SEM images of  $\text{MS}_2$  ( $\text{FeS}_2$ ,  $\text{CoS}_2$  and  $\text{NiS}_2$ ) and  $\text{MoS}_2$  samples.

DMF by sonication. The slurry was spread onto pretreated FTO glass. After air-drying, the working electrode was further dried at 393 K for 1 h to improve adhesion. Then, the Scotch tape was unstuck, and the uncoated part of the electrode was isolated with epoxy resin. All the photoelectrochemical measurements were carried out in 0.2 M  $\text{NaSO}_4$  aqueous solution, which was irradiated by simulated solar light (Shenzhen ShengKang Technology Co., Ltd, China, LX300F).

## 2.6. Photocatalytic test

The photocatalytic hydrogen production reaction was carried in a Pyrex top-irradiation reactor connected to a glass closed gas system at room temperature. In the photocatalytic experiment, 50 mg of catalyst powder was dispersed in an aqueous solution (100 mL) containing methanol (10 vol. %) as sacrificial electron donor. A 300 W Xeon lamp with a working current of 15 A (Shenzhen ShengKang Technology Co., Ltd, China, LX300 F) was used as a light source. The evolved gases were analyzed by gas chromatography using a thermal conductive detector (TCD).

## 3. Results and discussion

### 3.1. Photocatalyst characterization

The  $\text{MoS}_2$  and PyP samples were characterized by X-ray diffraction (XRD) displayed in Fig. 1a. It can be observed that only broad diffraction peaks can be found in the XRD patterns of PyP, indicating that the amorphous structure of the as-prepared pyrene-based polymer. All the diffraction peaks of pure  $\text{MoS}_2$  are termed as hexagonal structure of typical  $\text{MoS}_2$  [JCPDS card no. 73-1508] [25b]. There are no  $\text{MoS}_2$  signals appeared in the diffractions of x wt. %  $\text{MoS}_2/\text{PyP}(\text{IM})$  samples because of the little loading and the weak diffraction peaks of  $\text{MoS}_2$ . All the XRD patterns of x wt. %  $\text{MoS}_2/\text{PyP}(\text{IM})$  samples only displays one main broad peak at  $21.8^\circ$ . After modification with  $\text{MoS}_2$ , there are no obvious structure change can be observed. So we can conclude that deposition with  $\text{MoS}_2$  did not alter the characteristic functional group features of PyP.

The Raman spectra (Fig. 1b) and Fourier-transform spectra (FT-IR, Fig. 1c) provide good supporting evidence for this conclusion. All Raman spectrum of x wt. %  $\text{MoS}_2/\text{PyP}(\text{IM})$  samples displays three main

peaks: the characteristic bands of aromatic pyrene polycycles at  $1620\text{ cm}^{-1}$  and  $1350\text{ cm}^{-1}$ , the C–H stretching at  $1260\text{ cm}^{-1}$  and  $3200\text{ cm}^{-1}$ , respectively [32]. No evident difference in the band position of  $\text{MoS}_2/\text{PyP}$  can be viewed in comparison with pure PyP. In the FT-IR spectra of  $\text{MoS}_2/\text{PyP}(\text{IM})$ , the feature-distinctive stretch modes of aromatic ring C=C are centered at  $1250$  to  $1620\text{ cm}^{-1}$ , the C–H variations are located at  $650$  to  $1230\text{ cm}^{-1}$  and  $3050\text{ cm}^{-1}$ , which are in good accordance with pristine PyP. As shown in Fig. 1c, the characteristic peaks of  $\text{MoS}_2$  are mainly located at  $\sim 1500\text{ cm}^{-1}$ , which is quite close to the aromatic ring vibrations of PyP [32c]. The vibrations of the  $\text{MoS}_2$  are hardly observed in the  $\text{MoS}_2/\text{PyP}$ , presumably due to the overlap of the band with that of the aromatic ring vibrations. This meaning structural effect of PyP is ruled out in improving the hydrogen production performance.

The low temperature  $\text{N}_2$  BET analysis of pure PyP and  $\text{MoS}_2/\text{PyP}(\text{IM})$  samples was investigated. Fig. 1d shows a typical IV isotherm featuring with a pronounced H1-type hysteresis loop for polymer networks, supporting the surface area of the samples. The BET surface areas of pure PyP and  $\text{MoS}_2$  are respectively determined as  $710$  and  $16.5\text{ m}^2\text{ g}^{-1}$ , while that of the  $\text{MoS}_2/\text{PyP}(\text{IM})$  samples is  $658\text{ m}^2\text{ g}^{-1}$ . Compared with pure PyP, the modified sample exhibits slightly decreased specific surface area because of the mild agglomeration of PyP in the immersion.

Other transition metal sulfides ( $\text{FeS}_2$ ,  $\text{CoS}_2$  and  $\text{NiS}_2$ ) obtained by similar hydrothermal were characterized by XRD patterns (Fig. 2). Obviously, the diffraction peaks belonging to pure  $\text{MS}_2$  could be observed in the XRD patterns of  $\text{MS}_2/\text{PyP}(\text{IM})$  which is different from that of  $\text{MoS}_2/\text{PyP}(\text{IM})$ . Maybe the reason is  $\text{MS}_2$  with better crystallinity lead to stronger diffraction peak intensity than the former.

Field emission scanning electron microscopy (SEM) and high-resolution scanning transmission electron microscope (TEM) measurements were used to explore the morphologies of  $\text{MoS}_2/\text{PyP}(\text{IM})$  subsequently. SEM of pure PyP (Fig. 3a) shows a small particle size almost  $40$ – $100\text{ nm}$  while  $\text{MoS}_2$  nanosheets (Fig. 3b) show  $\sim 100\text{ nm}$  in y axis and a few nanometers in thickness. From the SEM image of  $\text{MoS}_2/\text{PyP}$  sample in Fig. 3c,  $\text{MoS}_2$  could be distinguished from PyP because of the obvious different morphology. TEM image of the 3 wt. %  $\text{MoS}_2/\text{PyP}(\text{IM})$  in Fig. 3d shows that  $\text{MoS}_2$  with a typical layered structure are distributed on the surface of PyP. The high-resolution TEM (HR-TEM) image of  $\text{MoS}_2$  displays a lattice fringe with  $d$ -spacing of  $0.62\text{ nm}$  (Fig. 3d) corresponding to the (002) plane of hexagonal structure, which is identified with XRD pattern. All the above characterizations reveal that  $\text{MoS}_2$  is successfully loaded on PyP using the simple synthetic approach. SEM of other transition metal sulfides ( $\text{FeS}_2$ ,  $\text{CoS}_2$  and  $\text{NiS}_2$ ) shows the morphologies of  $\text{MS}_2$  were blocky while  $\text{MoS}_2$  are multiple layered nanoflowers (Fig. 4).

The chemical states of  $\text{MoS}_2/\text{PyP}(\text{IM})$  were examined by X-ray photoemission spectroscopy (XPS) (Fig. 5). The binding energy at  $284.6\text{ eV}$  is ascribed to C–C, C=C & C–H of PyP. The patterns revealed that the Mo/S atomic ratio of  $1:2.09$ , in good agreement with the previous reports. [25] The binding energies of the Mo  $3d_{5/2}$  and Mo  $3d_{3/2}$  peaks located at  $229.7$  and  $232.9\text{ eV}$ , S 2s band at  $226.8\text{ eV}$ , respectively, demonstrating the values of  $\text{Mo}^{4+}$  and  $\text{S}^{2-}$  in  $\text{MoS}_2$ . The other two weak peaks at  $234.6$  and  $231\text{ eV}$  is assigned to the value of  $\text{Mo}^{5+}$ , presumably owing to the small amount of surface oxidation. [33] S 2p bands at  $163.6$  and  $162.5\text{ eV}$ , respectively, further confirmed the dominant existence of  $\text{S}^{2-}$  [25c]. Compared to pure  $\text{MoS}_2$ , the peaks in  $\text{MoS}_2/\text{PyP}(\text{IM})$  positively shifted with respect to the corresponding peaks because the strong interaction between PyP and  $\text{MoS}_2$  could indirectly weaken the Mo–S bonds by decreasing the electron density around S atoms in  $\text{MoS}_2$  [34].

The optical features of the  $\text{MoS}_2/\text{PyP}(\text{IM})$  were assessed by UV–vis spectroscopy and photoluminescence, electron paramagnetic resonance (EPR) spectra, and electrochemical impedance spectroscopy (EIS). In Fig. 6a, as expected, the DRS spectra of  $\text{MoS}_2/\text{PyP}(\text{IM})$  revealed a red shift in the optical absorption onset indicating broaden the light

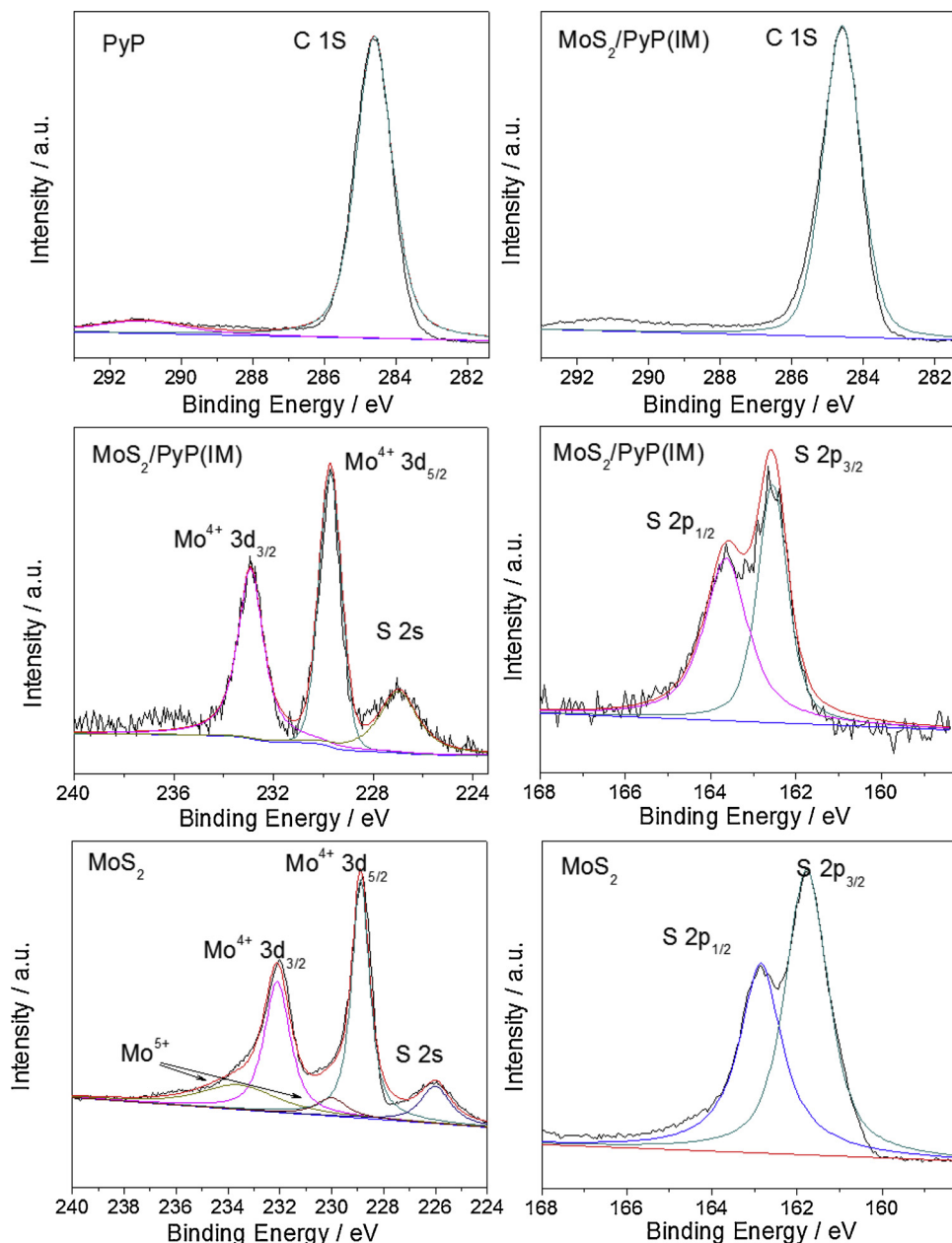


Fig. 5. High-resolution XPS spectra of C 1s, Mo 3d, and S 2p of pure PyP, MoS<sub>2</sub> and MoS<sub>2</sub>/PyP(IM) samples.

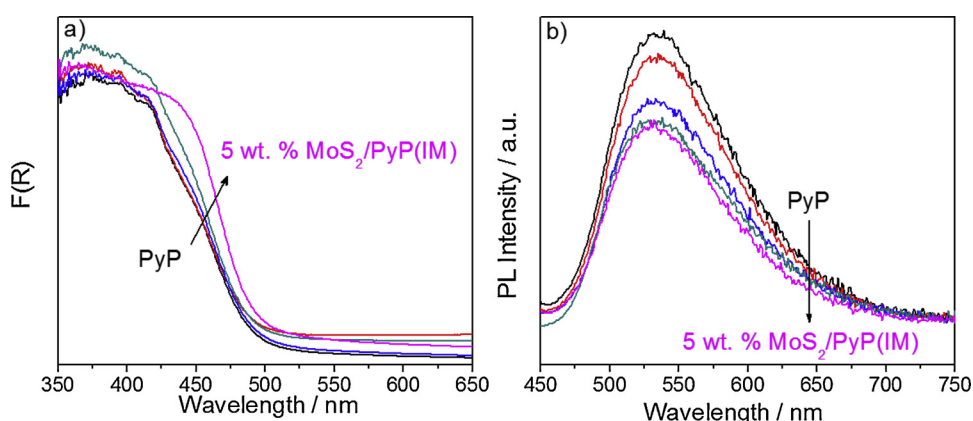
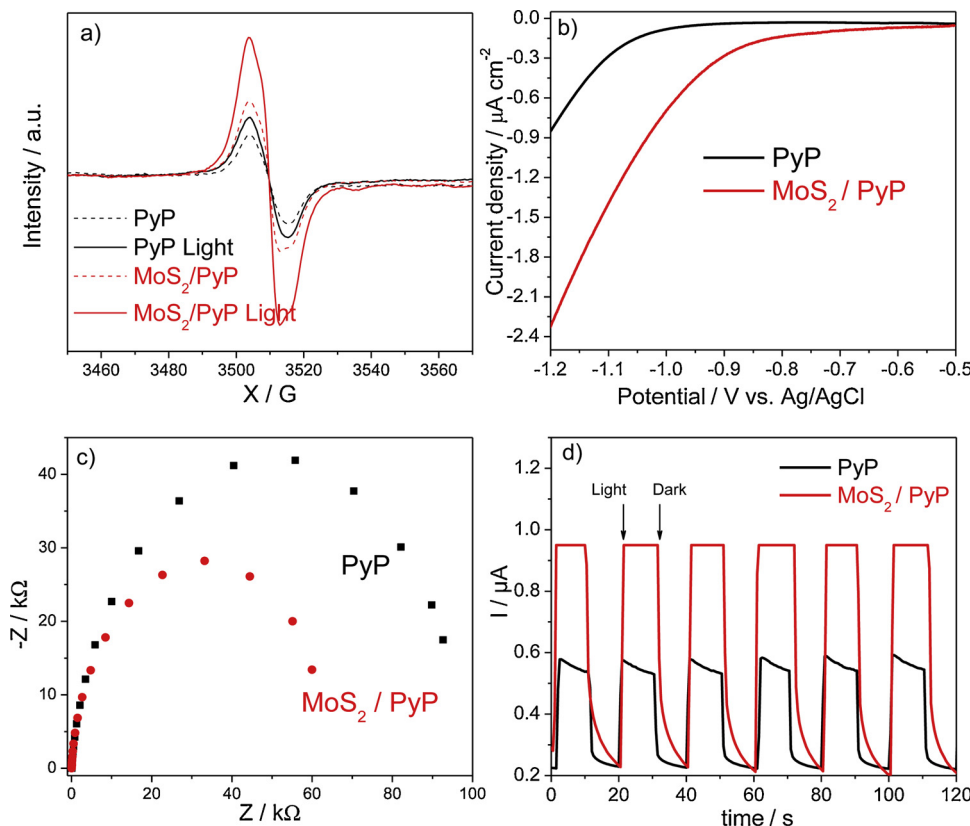
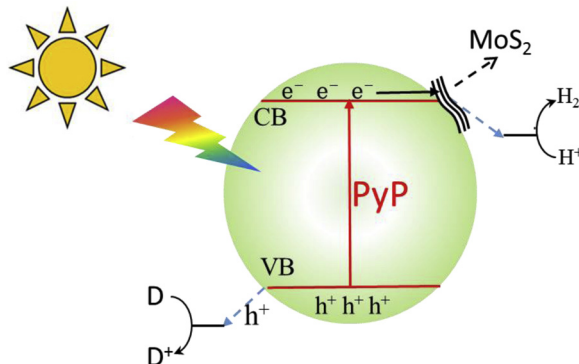


Fig. 6. Semiconductive optical features (a) UV-vis diffuse reflectance spectra, (b) PL spectra of x wt. % MoS<sub>2</sub>/PyP(IM) samples.



**Fig. 7.** a) Room temperature EPR spectra; Photoelectrochemical properties b) Polarization curves, c) Electrochemical impedance spectroscopy plots in the dark, d) Periodic on/off photocurrent response under visible-light irradiation ( $\lambda > 420 \text{ nm}$ ) at 0.4 V bias potential vs. Ag/AgCl in a 0.2 M Na<sub>2</sub>SO<sub>4</sub> aqueous solution of pure PyP and 3 wt. % MoS<sub>2</sub>/PyP(IM) samples.



**Scheme 1.** Schematic illustration of the between PyP and MoS<sub>2</sub>. D = donor.

absorbance. This is because MoS<sub>2</sub> with black color has strong optical absorption in the visible light region. The separation/recombination rates of the photo-excited electron-hole pairs of the samples were next investigated by PL spectra. As shown in Fig. 6b, a strong PL emission peak can be observed for the pristine PyP due to the radiative recombination of charge carriers. The PL quenching in these MoS<sub>2</sub>/PyP (IM) samples occurs in a saturated emission at 534 nm. It is attributed to the efficient charge transfer at the photoactive MoS<sub>2</sub>/PyP(IM) interface and further improved the separation efficiency of the photo-generated charge carriers.

There is one signal Lorentzian line of EPR spectrum centered at a *g*-factor value of 2.0032 were detected for PyP and MoS<sub>2</sub>/PyP(IM) respectively, indicating an unpaired electron on the  $\pi$ -conjugated PyP aromatic rings (Fig. 7a). Compared with pure PyP, the Lorentzian line of MoS<sub>2</sub>/PyP(IM) samples was enhanced obviously, presumably because of the redistribution of  $\pi$ -electrons within the hybrid by band offsets. Thus, the heterostructure is beneficial to optimize the electronic band structure for charge migration and separation. The EPR signals of

both PyP and MoS<sub>2</sub>/PyP(IM) samples were further increased under visible light irradiation illustrating the generation of unpaired electrons on the  $\pi$ -conjugated aromatic rings and efficient photo-induced generation of charge carrier pairs.

Electrochemical impedance spectra (EIS) were carried out to follow the charge separation and transfer efficiency of photogenerated electrons and holes in the well-developed MoS<sub>2</sub>/PyP(IM) material using a typical three-electrode cell. As shown in Fig. 7b, polarization curves recorded with the MoS<sub>2</sub> optimized PyP on FTO glass showed a smaller overpotential for the HER than pure PyP, which benefits by more active edge sites and the electrons trapped by MoS<sub>2</sub> nanosheets are easier to react with H<sup>+</sup> to produce H<sub>2</sub>. Electrochemical impedance spectroscopy displayed in Fig. 7c indicates the charge transfer rate in the dark. Obviously, MoS<sub>2</sub>/PyP(IM) shows a smaller arc radius and a lower resistance in charge transportation than that of pure PyP, which is benefited for superior charge separation of photogenerated e<sup>-</sup>-h<sup>+</sup> pairs. Fig. 7d showed prompt transient photocurrent response of the samples. After decorating PyP with MoS<sub>2</sub>, the increased photocurrent response reflect that photoinduced e<sup>-</sup>-h<sup>+</sup> pairs are separated more efficiently, further indicating the efficient transfer of charge carriers. The increase of photocurrent is also due to the enhanced visible light absorption of MoS<sub>2</sub>/PyP(IM). Therefore, we can conclude that construction of MoS<sub>2</sub>/PyP(IM) has improved photocatalytic-water-reduction kinetics compared to the pristine PyP and a better photocatalytic performance can be expected.

From the above analysis, a possible photocatalytic mechanism of the samples in HER is proposed briefly. Under visible light irradiation, the excited electrons generated on conduction band of PyP could rapidly transfer to MoS<sub>2</sub> with plenty of active sites. Meanwhile the holes generated at valence band of PyP would quickly move in a different direction and could be trapped by methanol (Scheme 1). On the one hand, the construction of the MoS<sub>2</sub>/PyP heterojunction can significantly restrain the charge recombination; on the other hand, MoS<sub>2</sub> as an electron receiver features plenty of active sites for HER thus improves the proton

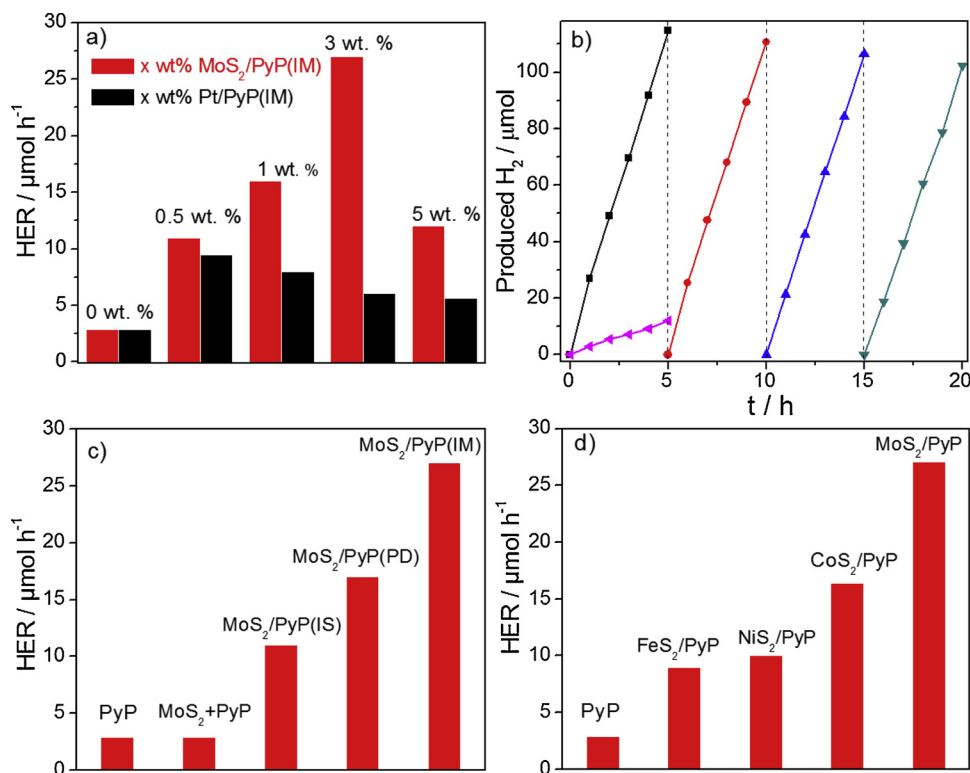


**Fig. 8.** Photocatalytic  $\text{H}_2$  evolution curves ( $\lambda \geq 420 \text{ nm}$ ) of a)  $\text{x}$  wt%  $\text{MoS}_2/\text{PyP(IM)}$  samples; b) Stability test of  $\text{H}_2$  evolution (evacuation every 5 h) for 3 wt%  $\text{MoS}_2/\text{PyP(IM)}$  samples; c) 3 wt%  $\text{MoS}_2/\text{PyP}$  samples by different synthesis method; d) 3 wt%  $\text{MS}_2/\text{PyP(IM)}$  samples produced by immersion.

reduction process.

### 3.2. Photocatalytic performance

Finally, the photocatalytic  $\text{H}_2$  production activity on  $\text{x}$  wt%  $\text{MoS}_2/\text{PyP(IM)}$  composites were evaluated under xenon arc lamp irradiation using methanol as a scavenger (Fig. 8a). Pristine PyP shows mild photocatalytic activity because of the rapid recombination of photo-generated carrier and few active sites. The introduction of layered  $\text{MoS}_2$  makes a significant improvement of PyP in photocatalytic water splitting to  $\text{H}_2$ . Fig. 8a shows a typical volcano relationship between hydrogen-evolution-activity and loading contents. Firstly, gradual increase in the hydrogen evolution rate takes place when the incorporation amounts of  $\text{MoS}_2$  were increased from 0.5 wt% to 3 wt%. The optimum hydrogen-evolution rate over 3.0 wt%  $\text{MoS}_2/\text{PyP(IM)}$  reaches  $27 \mu\text{mol h}^{-1}$ . The photocatalytic activity of samples decreased while further increasing the amount of  $\text{MoS}_2$  in the PyP because of the shading effects that seriously block the incident light absorption of PyP [35,21c]. In addition, when the  $\text{MoS}_2$  alone under the experimental conditions, no appreciable  $\text{H}_2$  was detected, suggesting that  $\text{MoS}_2$  is incapable acted as a photocatalyst for photocatalytic  $\text{H}_2$  production. This result further confirms that the improved photocatalytic performance was profited from the construction of  $\text{MoS}_2/\text{PyP}$  heterostructure. Compared with traditional cocatalyst Pt, the optimum hydrogen evolution rate over  $\text{MoS}_2/\text{PyP(IM)}$  reaches  $27 \mu\text{mol h}^{-1}$  which is ~3-time higher than that of  $\text{Pt/PyP}$ . This result reveals that the construction of  $\text{MoS}_2/\text{PyP}$  heterojunction has a good performance than that of noble metal Pt in photocatalytic water reduction.

Fig. 8b shows prolonged irradiation with visible light for four cycles lasting 20 h (5 h per cycle). The hydrogen evolution rate of the catalyst did not show evident decrease in the activity, indicating its high stability during photocatalytic  $\text{H}_2$  evolution [27c]. The total amount of  $\text{H}_2$  in the first cycle was  $115 \mu\text{mol}$ , much more than that of pure PyP ( $12 \mu\text{mol}$ ). For comparison, Fig. 8c shows the photocatalytic hydrogen

evolution over the optimal  $\text{MoS}_2/\text{PyP(IS)}$ ,  $\text{MoS}_2/\text{PyP(PD)}$  and  $\text{MoS}_2 + \text{PyP}$  synthesized via the widely reported methods including in-situ, photodeposition and physical mixing. The modification of  $\text{MoS}_2/\text{PyP}$  by different methods (IS or PD) displays further improved photoactivity for  $\text{H}_2$  evolution, while  $\text{MoS}_2 + \text{PyP}$  physical mixture shows no increase in the activity. The hydrogen evolution rate of 3 wt%  $\text{MoS}_2/\text{PyP(IS)}$  and  $\text{MoS}_2/\text{PyP(PD)}$  is  $11$  and  $17 \mu\text{mol h}^{-1}$ , respectively, while that of  $\text{MoS}_2/\text{PyP(IM)}$  is  $27 \mu\text{mol h}^{-1}$ . The result implies that the immersion method is more beneficial than the other two fabrication technique (in-situ and photodeposition) in loading  $\text{MoS}_2$  onto the PyP for the photocatalytic water splitting to  $\text{H}_2$ . The effect of other transition metal sulfides ( $\text{FeS}_2$ ,  $\text{CoS}_2$ ,  $\text{NiS}_2$ ) for PyP are also measured for the comparison. Results in Fig. 8d reveal that all the as-prepared composites show good photocatalytic  $\text{H}_2$  production activities, while the optimum activity was achieved when  $\text{MoS}_2$  was used to construct the heterojunction. This is mainly ascribed to the layered structure of  $\text{MoS}_2$  superior to the blocky of other  $\text{MS}_2$  which means the layered  $\text{MoS}_2$  can greatly matched with PyP, facilitating charge transfer and finally shows the optimum activity. However, the varying degrees of improvement revealed that the construction of heterojunctions by transition metal sulfides with PyP ( $\text{MS}_2/\text{PyP}$ ) can efficiently facilitate the  $\text{H}_2$  production process.

### 4. Conclusion

In summary, the well-developed  $\text{MS}_2/\text{PyP}$  heterojunctions by different fabrication techniques (immersion, photodeposition and in-situ methods) and various transition metal sulfides ( $\text{MoS}_2$ ,  $\text{FeS}_2$ ,  $\text{CoS}_2$ ,  $\text{NiS}_2$ ) can serve as efficient photocatalysts for  $\text{H}_2$  production. Characterization revealed that the successful construction of heterojunctions can efficiently suppress charge recombination, improve interfacial charge transfer, and provide more active adsorption sites and photocatalytic reaction centers. This study attests the PyP with  $\pi$ -conjugated group used for photocatalytic  $\text{H}_2$  evolution is therefore of great significance.

We believe a timely study of the pyrene-based conjugated polymers as emerging heterogeneous photocatalysts would stimulate the investigations for other photocatalytic applications, such as CO<sub>2</sub> reduction, phenol synthesis from benzene, and the selective oxidation of aromatic alcohols.

## Acknowledgements

This work was financially supported by the National Key Technologies R & D Program of China (2018YFA0209301), the National Natural Science Foundation of China (21425309, 21761132002 and 21861130353), the 111 Project (D16008), and the Chang Jiang Scholars Program of China (T2016147).

## References

- [1] (a) A.J. Bard, M.A. Fox, *Acc. Chem. Res.* 28 (1995) 141–145; (b) A. Fujishima, K. Honda, *Nature* 238 (1972) 37–38; (c) T. Hisatomi, J. Kubota, K. Domen, *Chem. Soc. Rev.* 43 (2014) 7520–7535.
- [2] (a) N.S. Lewis, D.G. Nocera, *Proc. Natl. Acad. Sci. U. S. A.* 103 (2006) 15729–15735; (b) A. Kudo, Y. Miseki, *Chem. Soc. Rev.* 38 (2009) 253–278; (c) K. Maeda, K. Domen, *J. Phys. Chem. Lett.* 1 (2010) 2655–2661.
- [3] (a) M. Pelaez, N.T. Nolan, S.C. Pillai, M.K. Seery, P. Falaras, A.G. Kontos, P.S.M. Dunlop, J.W.J. Hamilton, J.A. Byrne, K. O'Shea, M.H. Entezari, D.D. Dionysiou, *Appl. Catal. B* 125 (2012) 331–349; (b) Y. Kageshima, T. Minegishi, Y. Goto, H. Kaneko, K. Domen, *Sustain. Energy Fuels* 2 (2018) 1957–1965.
- [4] (a) G. Yu, J. Gao, J.C. Hummelen, F. Wudl, A.J. Heeger, *Science* 270 (1995) 1789–1791; (b) X. Li, J. Yu, M. Jaroniec, *Chem. Soc. Rev.* 45 (2016) 2603–2636; (c) G.G. Zhang, Z.A. Lan, X.C. Wang, *Angew. Chem. Int. Ed.* 55 (2016) 15712–15727.
- [5] (a) H. Friend, R.W. Gymer, A.B. Holmes, J.H. Burroughes, R.N. Marks, C. Taliani, D.C. Bradley, D.A.D. Santos, J.L. Brédas, M. Lögdlund, W.R. Salaneck, *Nature* 397 (1999) 121–128; (b) D.L. Jiang, C.K. Choi, K. Honda, W.S. Li, T. Yuzawa, T. Aida, *J. Am. Chem. Soc.* 126 (2004) 12084–12089.
- [6] (a) E. Smela, J. Micromech. Microeng. 9 (1999) 1–18; (b) T. Hasell, A.I. Cooper, *Nat. Rev. Mater.* 1 (2016) 16053–16156.
- [7] D.T. McQuade, A.E.T. Pullen, M. Swager, *Chem. Rev.* 100 (2000) 2537–2574.
- [8] (a) S. Yanagida, A. Kabumoto, K. Mizumoto, C. Pac, K. Yoshino, *J. Chem. Soc. Chem. Commun.* 8 (1985) 474–475; (b) P. Kuhn, A. Forget, D.S. Su, A. Thomas, M. Antonietti, *J. Am. Chem. Soc.* 130 (2008) 13333–13337; (c) Shibata, A. Kabumoto, T. Shiragami, O. Ishitani, C. Pac, S. Yanagida, *J. Phys. Chem.* 94 (1990) 2068–2076.
- [9] (a) X. Wang, K. Maeda, A. Thomas, K. Takanabe, G. Xin, J.M. Carlsson, K. Domen, M. Antonietti, *Nat. Mater.* 8 (2009) 76–82; (b) D. Zheng, X.N. Cao, X.C. Wang, *Angew. Chem. Int. Ed.* 55 (2016) 11512–11516; (c) G.X. Zhao, H. Pang, G.G. Liu, P. Li, H.M. Liu, H.B. Zhang, L. Shi, J.H. Ye, *Appl. Catal. B* 200 (2017) 141–149; (d) G.G. Zhang, G.S. Li, T. Heil, S. Zafeiratos, F.L. Lai, A. Savateev, M. Antonietti, X.C. Wang, *Angew. Chem. Int. Ed.* 58 (2019) 3433–3437.
- [10] (a) M. Ledendecker, S.K. Calderón, C. Papp, H.P. Steinrück, M. Antonietti, M. Shalom, *Angew. Chem. Int. Ed.* 54 (2015) 12361–12365; (b) G.G. Zhang, L.H. Lin, G.S. Li, Y.F. Zhang, A. Savateev, S. Zafeiratos, X. Wang, M. Antonietti, *Angew. Chem. Int. Ed.* 57 (2018) 9372–9376.
- [11] (a) R.S. Sprick, J.X. Jiang, B. Bonillo, S. Ren, T. Ratjavitvech, P. Guiglion, M.A. Zwijnenburg, D.J. Adams, A.I. Cooper, *J. Am. Chem. Soc.* 137 (2015) 3265–3270; (b) C.S. Pan, T. Takata, M. Nakabayashi, T. Matsumoto, N. Shibata, Y. Ikuhara, K. Domen, *Angew. Chem. Int. Ed.* 54 (2015) 2955–2959; (c) R.S. Sprick, B. Bonillo, R. Clowes, P. Guiglion, N.J. Brownbill, B.J. Slater, F. Blanc, M.A. Zwijnenburg, D.J. Adams, A.I. Cooper, *Angew. Chem. Int. Ed.* 55 (2016) 1792–1796.
- [12] (a) Y.W. Su, W.H. Lin, Y.J. Hsu, K.H. Wei, *Small* 10 (2014) 4427–4442; (b) S. Melissen, T.L. Bahers, S.N. Steinmann, P. Sautet, *J. Phys. Chem. C* 119 (2015) 25188–25196; (c) J. Chen, C. Dong, D. Zhao, Y. Huang, X. Wang, L. Samad, L. Dang, M. Shearer, S. Shen, L. Guo, *Adv. Mater.* 29 (2017) 1606198.
- [13] (a) Z. Zhang, J. Long, L. Yang, W. Chen, W. Dai, X. Fu, X. Wang, *Chem. Sci.* 2 (2011) 1826–1830; (b) K. Kailasam, J. Schmidt, H. Bildirir, G. Zhang, S. Blechert, X. Wang, A. Thomas, *Macromol. Rapid Commun.* 34 (2013) 1008–1013.
- [14] (a) M. Svensson, F. Zhang, S.C. Veenstra, W.J.H. Verhees, J.C. Hummelen, J.M. Kroon, O. Ingan, M.R. Andersson, *Adv. Mater.* 15 (2003) 988–991; (b) M.H. Chen, J. Hou, Z. Hong, G. Yang, S. Sista, L.M. Chen, Y. Yang, *Adv. Mater.* 21 (2009) 4238–4242; (c) R.S. Sprick, B. Bonillo, M. Sachs, R. Clowes, J.R. Durrant, D.J. Adams, A.I. Cooper, *Chem. Commun. (Camb.)* 52 (2016) 10008–10011.
- [15] (a) L.W. Li, Z.X. Cai, Q.H. Wu, W. Lo, N. Zhang, L.X. Chen, L.P. Yu, *J. Am. Chem. Soc.* 138 (2016) 7681–7686; (b) X.L. Yang, Y.G. Xiang, X.P. Wang, S. Li, H. Chen, X. Ding, *Catalysts* 8 (2018) 185–199; (c) L. Stegbauer, S. Zech, G. Savasci, T. Banerjee, F. Podjaski, K. Schwinghammer, C. Ochsenfeld, B.V. Lotsch, *Adv. Energy Mater.* 8 (2018) 1703278.
- [16] (a) K. Zhang, D. Kopetzki, P.H. Seeberger, M. Antonietti, F. Vilela, *Angew. Chem. Int. Ed.* 52 (2013) 1432–1436; (b) C. Yang, B.C. Ma, L.Z. Zhang, S. Lin, S. Ghasimi, K. Landfester, K.A.I. Zhang, X.C. Wang, *Angew. Chem. Int. Ed.* 55 (2016) 9202–9206; (c) C.H.A. Tsang, J. Tobin, J. Xuan, F. Vilela, H.B. Huang, D.Y.C. Leung, *Appl. Catal. B* 240 (2019) 50–63.
- [17] (a) M.S. Zhu, Y.T. Lu, Y.K. Du, J. Li, X.M. Wang, P. Yang, *Int. J. Hydrogen Energy* 36 (2011) 4298–4304; (b) R.S. Sprick, C.M. Aitchison, E. Berardo, L. Turcani, L. Wilbraham, B.M. Alston, K.E. Jelfs, M.A. Zwijnenburg, A.I. Cooper, J. Mater. Chem. A Mater. Energy Sustain. 6 (2018) 11994–12003.
- [18] (a) M. Shalom, S. Gimenez, F. Schipper, I.H. Cardona, J. Bisquert, M. Antonietti, *Angew. Chem. Int. Ed.* 126 (2014) 3728–3732; (b) M.F. Zheng, J.L. Shi, T. Yuan, X.C. Wang, *Angew. Chem. Int. Ed.* 57 (2018) 5487–5491; (c) B. Kurpil, K. Otte, M. Antonietti, A. Savateev, *Appl. Catal. B* 228 (2018) 97–102.
- [19] (a) J. Yu, S. Wang, B. Cheng, Z. Lin, F. Huang, *Catal. Sci. Technol.* 3 (2013) 1782–1789; (b) S.P. Adhikari, Z.D. Hood, V.W. Chen, K.L. More, K. Senevirathne, A. Lachgar, *Sustain. Energy Fuels* 2 (2018) 2507–2515; (c) G.G. Zhang, S.H. Zang, Z.A. Lan, C.J. Huang, G.S. Li, X.C. Wang, *J. Mater. Chem. A Mater. Energy Sustain.* 3 (2015) 17946–17950.
- [20] (a) J.G. Hou, H.J. Cheng, O. Takeda, H.M. Zhu, *Energy Environ. Sci.* 8 (2015) 1348–1357; (b) S.W. Cao, J.X. Low, J.G. Yu, M. Jaroniec, *Adv. Mater.* 27 (2015) 2150–2176; (c) Z. Zhu, Z. Lu, D. Wang, X. Tang, Y. Yan, W. Shi, N. Cao, X. Yao, H. Dong, *Appl. Catal. B* 182 (2016) 115–122.
- [21] (a) F.T. Yu, Z.Q. Wang, S.C. Zhang, H.N. Ye, K.Y. Kong, X.Q. Gong, J.L. Hua, H. Tian, *Adv. Funct. Mater.* 28 (2018) 1804512; (b) J.H. Qiu, X.G. Zhang, Y. Feng, X.F. Zhang, H.T. Wang, J.F. Yao, *Appl. Catal. B* 231 (2018) 317–342.
- [22] (a) Q. Wang, Y. Li, T. Hisatomi, M. Nakabayashi, N. Shibata, J. Kubota, K. Domen, *J. Catal.* 328 (2015) 308–315; (b) Q. Wang, T. Hisatomi, Q. Jia, H. Tokudome, M. Zhong, C. Wang, Z. Pan, T. Takata, M. Nakabayashi, N. Shibata, Y. Li, I. Sharp, A. Kudo, T. Yamada, K. Domen, *Nat. Mater.* 15 (2016) 611–615.
- [23] (a) S.J.A. Moniz, S.A. Shevlin, D.J. Martin, Z.X. Guo, J.W. Tang, *Energy Environ. Sci.* 8 (2015) 731–759; (b) M. Zhao, H.H. Li, X.P. Shen, *Acta Chim. Sin.* 74 (2016) 825–832; (c) Y. Chen, G. Jia, Y.F. Hu, G.Z. Fan, Y.H. Tsang, Z.S. Li, Z.G. Zou, *Sustain. Energy Fuels* 1 (2017) 1875–1898; (d) Y.Q. Zhu, M.W. Shah, C.Y. Wang, *Appl. Catal. B* 203 (2017) 526–532.
- [24] (a) S. Wang, X. Wang, *Appl. Catal. B* 162 (2015) 494–500; (b) K. Chang, X. Hai, J.H. Ye, *Adv. Energy Mater.* 6 (2016) 1502555.
- [25] (a) K. Sakamaki, K. Hinokuma, A. Fujishima, *J. Vac. Sci. Technol. B* 9 (1991) 944–949; (b) J.F. Xie, H. Zhang, S. Li, R.X. Wang, X. Sun, M. Zhou, J.F. Zhou, X.W. Lou, Y. Xie, *Adv. Mater.* 25 (2013) 5807–5813; (c) X.M. Geng, W.W. Sun, W. Wu, B. Chen, A. Al-Hilo, M. Benamara, H.L. Zhu, F. Watanabe, J.B. Cui, T.P. Chen, *Nat. Commun.* 7 (2016) 10672; (d) Y.P. Liu, Y.H. Li, F. Peng, Y. Lin, S.Y. Yang, S.S. Zhang, H.J. Wang, Y.H. Cao, H. Yuan, *Appl. Catal. B* 241 (2019) 236–245.
- [26] (a) Q.J. Xiang, J.G. Yu, M. Jaroniec, *J. Am. Chem. Soc.* 134 (2012) 6575–6578; (b) W. Zhou, Z. Yin, Y. Du, X. Huang, Z. Zeng, Z. Fan, H. Liu, J. Wang, H. Zhang, *Small* 9 (2013) 140–147.
- [27] (a) X. Zong, H.J. Yan, G.P. Wu, G.J. Ma, F.Y. Wen, L. Wang, C. Li, *J. Am. Chem. Soc.* 130 (2008) 7176–7177; (b) J. Zhang, Z.P. Zhu, X.L. Feng, *Chem. Eur. J.* 20 (2014) 10632–10635; (c) K. Chang, Z.W. Mei, T. Wang, Q. Kang, S.X. Ouyang, J.H. Ye, *ACS Nano* 8 (2014) 7078–7087.
- [28] (a) Y.G. Li, H.L. Wang, L.M. Xie, Y.Y. Liang, G.S. Hong, H.J. Dai, *J. Am. Chem. Soc.* 133 (2011) 7296–7299; (b) U. Maitra, U. Gupta, M. De, R. Datta, A. Govindaraj, C.N.R. Rao, *Angew. Chem. Int. Ed.* 52 (2013) 13057–13061; (c) Q.J. Xiang, J.G. Yu, M. Jaroniec, *J. Am. Chem. Soc.* 134 (2012) 6575–6578.
- [29] (a) Y.D. Hou, A.B. Laursen, J.S. Zhang, G.G. Zhang, Y.S. Zhu, X.C. Wang, S. Chorkendorff, *Angew. Chem. Int. Ed.* 125 (2013) 3709–3713. *Angew. Chem. Int. Ed.*, 52 (2013) 3621–3625; (b) D.D. Zheng, G.G. Zhang, Y.D. Hou, X.C. Wang, *Appl. Catal. A Gen.* 521 (2016) 2–8.
- [30] D. Genuit, A. Afanasiev, M. Vrinat, *J. Catal.* 235 (2005) 302–317.
- [31] (a) R.J. Bouchard, *J. Cryst. Growth* 2 (1968) 40–44; (b) F. Soofivand, E. Esmaeili, M. Sabet, M.S. Niasari, *J. Mater. Sci. Mater. Electron.* 29 (2018) 858–865.
- [32] (a) S.A. Asher, *Anal. Chem.* 56 (1984) 720–724; (b) T.J. Simmons, J. Bult, D.P. Hashim, R.J. Linhardt, P.M. Ajayan, *ACS Nano* 3 (2009) 865–870; (c) Q. Li, N. Zhang, Y. Yang, G.Z. Wang, D.H.L. Ng, *Langmuir* 30 (2014) 8965–8972.

[33] (a) W. Gruinert, A. Yu Stakheev, R. Feldhaus, K. Anders, E.S. Shpiro, K.M. Minachev, *J. Phys. Chem.* 95 (1991) 1323–1328;  
(b) L. Benoist, D. Gonbeau, G. Pfister-Guillouzo, E. Schmidt, G. Meunier, A. Levasseur, *Surf. Interface Anal.* 22 (1994) 206–210. *Thin Solid Films*, 258 (1995) 110-114.

[34] (a) J. Staszak-Jirkovsky, C.D. Malliakas, P.P. Lopes, N. Danilovic, S.S. Kota, K.C. Chang, B. Genorio, D. Strmcnik, V.R. Stamenkovic, M.G. Kanatzidis, N.M. Markovic, *Nat. Mater.* 15 (2016) 197–203;  
(b) H.Y. Jin, X. Liu, Y. Jiao, A. Vasileff, Y. Zheng, S.Z. Qiao, *Nano Energy* 53 (2018) 690–697.

[35] G.G. Zhang, S.H. Zang, X.C. Wang, *ACS Catal.* 5 (2015) 941–947.